Electrochimica Acta 453 (2023) 142341

Contents lists available at ScienceDirect

Electrochimica Acta

journal homepage: www.journals.elsevier.com/electrochimica-acta

New insights on the reaction mechanism and charge contribution of $NaNiF_3$ perovskite as an anode for sodium-ion batteries

Liliana T. López Ch [a], Alejandro Medina [b], Franklin Jaramillo [a], Jorge A. Calderón [a,*], Pedro Lavela [b], José L. Tirado [b]

[a] Centro de Investigación, Innovación y Desarrollo de Materiales CIDEMAT, Facultad de Ingeniería, Universidad de Antioquia, Calle 70 N° 52-21, Medellín, Colombia
[b] Departamento de Química Inorgánica e Ingeniería Química, Instituto Universitario de Investigación en Química Fina y Nanoquímica (IUNAN), grupo PAIDI FQM288 Química y Electroquímica de Materiales Inorgánicos (QUEMI). Universidad de Córdoba, Campus de Rabanales, Edificio Marie Curie, E-14071 Córdoba, España

ARTICLE INFO

Keywords:
$NaNiF_3$
Perovskite
Anode
Conversion mechanism
Sodium-ion batteries
Capacitive behavior

ABSTRACT

Sodium-ion battery is a growing technology that has become a major focus of attention for energy storage of smart electric grids and renewable energy because of the enormous availability of sodium and its low cost of production. Particularly, the perovskite structure is an attractive material due to its novel properties in energy applications, such as good ionic mobility, low cost, facile route of synthesis, and fabrication. In the present work, an electrode based on $NaNiF_3$ nanostructured perovskite active materials was explored as an anode for sodium-ion battery application. The morphology and microstructure of $NaNiF_3$ perovskite were optimized using trisodium citrate dehydrated and microwave heating. Here a remarkable first capacity of c.a. 376 mA h g^{-1} of the optimized electrode was obtained in the first discharge. The ex-situ XRD and electrochemical characterization of the active material allow proposing a reaction mechanism by conversion processes during the discharge and identifying a capacitive contribution of around 25% to the total current at 20 mV s^{-1}.

1. Introduction

Myriads of good ideas in the field of electrochemical energy storage appear every year. Most of them are sagaciously studied as fundamental research, but hardly ever find further development and implementation. An outstanding example of success is the lithium-ion battery (LIB) concept. The basics of this widely applied concept were developed more than thirty years ago when 2019's Nobel laureates in chemistry and a reduced group of other researchers boosted the possibilities of commercial production and real application of LIBs [1]. Since then, there have been incremental improvements of high relevance, but no quantum leap was achieved. More recently, a new impetus to the recovery of early forgotten alternatives, such as sodium-ion and multivalent metal batteries, was stimulated by geopolitical and economic concerns regarding lithium availability and cobalt abundance and cost, never forgetting the safety issues in which LIBs have been involved.

In this way, the parallel accelerating growth of public and private financial investments on these topics, as well as the progressive use of more and more sophisticated experimental techniques and large facilities have developed a particularly growing in sodium-ion batteries (SIBs). Since the early studies on sodium intercalation chemistry, primary sodium batteries, and the rocking-chair concept, SIBs are the closest alternative systems to practical application and partial LIB replacement. SIBs are an attractive technology for energy storage from renewable resources and for electricity distribution grids and home batteries, where energy density and volume can be less important than production costs and availability. This possibility has been recognized in excellent reviews [2–8]. These authors also emphasized the need for optimal electrode materials for SIBs development. There is a considerably large group of materials that have been used for applications for the cathode, such as layered oxides, NASICON phosphates, and metal fluorophosphates and fluorides, among others [5,9]. For the anode, carbon, intercalation materials, alloys, and conversion electrodes have been studied [6,10–13].

In recent years, halide perovskites have gained attention in battery applications due to their energy storage ability as 3D diffusion channels and tunable electrical properties of the structure, easy route of synthesis, and reduced production cost, among others [14–16]. Their nominal stoichiometry is ABX_3 where A can be an organic or an alkali or alkaline earth metal, B is a transition or post-transition metal, and X is a halogen.

* Corresponding author.
E-mail address: andres.calderon@udea.edu.co (J.A. Calderón).

https://doi.org/10.1016/j.electacta.2023.142341
Received 26 October 2022; Received in revised form 15 March 2023; Accepted 31 March 2023
Available online 31 March 2023

The ideal perovskite has a cubic Pm-3m structure formed by BX_6 octahedra sharing all corners with neighbor octahedra and defining X_{12} cavities where the larger A cation fits in cuboctahedric coordination and its structural stability is referred to as a semi-empirical factor knows as Goldschmidt's tolerance factor (*t*) [17]; in the case of the cubic structure, *t* is close to 1, while for those distorted structures *t* is comprised between 0.813-1.107. Alternatively, the structure can be described as an apparent cubic close packing of A and X atoms with one-fourth of the octahedral holes filled with A. Many distorted varieties from the cubic perovskite are also known. A particularly outstanding compound in recent years is the tetragonal I4/mcm $CH_3NH_3PbX_3$ (X: I, Br, and Cl) due to its promising applicability in solar cells and recent use in lithium-ion batteries (LIB) [17–21].

On the other hand, the $NaFeF_3$ compound has been explored for applications as LIB and SIB cathode materials, featuring a high open-circuit voltage close to 3.2 V and a good capacity of around 200 mA h g^{-1} [22–25]. However, the $NaFeF_3$ structure is far from the perovskite structure, being orthorhombic with layers of edge-sharing octahedra which define an interlayer space where sodium ions are in NaF_6 trigonal prismatic coordination. Other perovskites have been previously studied for sodium-ion as $NaMnF_3$, $NaNiF_3$, $NaCoF_3$, and others [24,26,27]. Nevertheless, these materials were tested mainly as cathodes and showed poor cyclability as well as low experimental capacity mostly below the theoretical value, which is close to 190 mA h g^{-1} [24]. The poor capacity of $NaNiF_3$ as a cathode is likely attributed to the low feasibility to carry out an intercalation reaction, because during the first charge process of the $NaNiF_3$ vs Na^+ release would be required and the consequent Ni oxidation to form NiF_3, which is an unstable compound, and promotes the formation of other more favorable species. Hence, the reversibility of the process and the intercalation of Na+ ions are lesser favorable. However, fluoride perovskites are versatile materials that can be used as conversion electrode materials, which commonly favor higher capacities [28].

For example, the theoretical capacity for the $NaNiF_3$ electrode through a full conversion reaction that forms Ni and NaF is close to 386.5 mA h g^{-1}. What could open an opportunity to explore this active material as an alternative anode to graphite which has a capacity close to 370 mA h g^{-1} [29], although the graphite presents hindrance for its extended use. It could promote short circuits during fast charging due to dendrite formation, besides the low potential of work that would promote lithium deposition. In particular, Ni, et al. [30] evaluated $NaNiF_3$ as an anode material of lithium-ion batteries with the incorporation of $NaNiF_3$ composite material which grows directly over the Ni foam. Here they obtained very interesting stability of cycling during 100 cycles with a capacity close to 0.15 mA h cm^{-2}. On the other hand, $NaNiF_3$ has seemingly shown capacitive behavior with a capacitance of around 1342 F g^{-1} at 5 A g^{-1} and good stability after cycling [31]. In this sense, $NaNiF_3$ is a singular material that what could be explored as an alternative anode of sodium and lithium-ion batteries. Besides, this material apparently could have faradaic and capacitive contribution to the total charge process.

In the present work, we have explored for the first time the $NaNiF_3$ electrode material as an anode for sodium-ion battery applications incorporating the use of microwave heating and sodium citrate to obtain a nanostructured active material. Its electrochemical behavior was evaluated, which exhibited a first discharge capacity of 376 mA h g^{-1}, close to its theoretical conversion capacity value. The mechanism of the $NaNiF_3$ electrode during the discharge was evaluated under XRD ex-situ analysis verifying a conversion reaction is carried out. Finally, the capacitive effect over the total stored charge was estimated, and here we observed a contribution of up to 25% at 20 mV s^{-1}.

2. Experimental section

The $NaNiF_3$ perovskite preparation consisted of a solvothermal process with the dissolution of $NiCl_2{\cdot}6H_2O$ (Nickel chloride hexahydrate) in ethylene glycol solvent. After that, stoichiometric amounts of NH_4F (ammonium fluoride) dissolved in distilled water and $NaC_2H_3O_2$ (sodium acetate anhydrous) were added with vigorous stirring. However, before adding $NaC_2H_3O_2$, $Na_3C_6H_5O_7{\cdot}2H_2O$ (three sodium citrate dehydrated) was incorporated as a carbon source for a conductive coating and to control $NaNiF_3$ particle size. Then, 1 h annealing treatment at 200°C was carried out in a microwave oven inside of a closed Teflon holder with permanent stirring at 600 rpm [27]. Here microwave heating was used due to it significantly reduces the time of synthesis compared with conventional heating [32]. After cooling, the solid product was removed by centrifugation and successively washed with ethanol three times combining centrifugation and an ultrasonic bath. This sample is labeled NNF+C due to sodium citrate incorporation. However, the crystallographic and morphologic characterization of a sample prepared in the absence of sodium citrate is reported to observe the different properties of a non-coated material. This sample is labeled as NNF (see Tables 1 and S1 and Figs. S1, S3 and S4). To the best of our knowledge, it was the first time $NaNiF_3$ perovskite was synthesized by using microwave heating.

Sample purity, unit cell parameters, and crystallinity were determined from X-ray powder diffraction (XRD), recorded in a BrukerD8 Discover A25 diffractometer, equipped with Cu Kα radiation, Ge monochromator, and Lynxeye detector. The patterns were scanned between 20 and 60° (2θ) with 0.01 °(2θ) step size and 1s step duration. Rietveld analyses were carried out with high score plus software, here the lattice parameters, crystallite size, and micro-strains are obtained and compared with the theoretical pattern. Ex-situ X-ray patterns of used electrodes were scanned between 20 and 60° (2θ) with 0.01° (2θ) step size and 0.45s step duration. Transmission electron microscopy (TEM) images were recorded in a Tecnai F20 Super Twin TMP microscope with a field emission power and resolution of 0.1 nm at 200 KV. Its maximum magnification is up to 1 MX. The camara used is a GATAN US 1000XP-P. Additionally elemental analysis was done with STEM - FISCHIONE Instruments M3000 FP5360/22 HAADF and Detector EDX Oxford Instruments XMAX. Field-emission scanning electron microscopy (FESEM) images was acquired in a JEOL JSM 6490LV microscope. X-ray photoelectron spectroscopy (XPS) was used to analyze the chemical composition and the oxidation state of nickel, sodium, and fluoride in pristine NNF+C in a SPECS Phobios 150 MCD spectrometer using an Al-Kα X-ray source. The sample was pelletized and outgassed to a high vacuum overnight. The binding energy scale was referred to the C1s line of adventitious carbon (284.6 eV).

The electrodes were composed of a mixture of active material, binder (polyvinylidene fluoride-PVDF), and carbon super p in a 70:15:15 ratio, respectively. They were dispersed by stirring in *N*-methyl-2-pyrrolidone (NMP) and pasted onto aluminum as a current collector at the beginning of the analysis however, after verifying the contribution of aluminum

Table 1
Elemental composition extracted from XPS measurements and crystallographic data from XRD patterns of the studied samples.

Element /Crystalline parameter	Sample		
	NNF	NNF+C	$NaNiF_3$ Pnma theoretical [33]
% Na	15.1	23.6	20
% Ni	20	23.6	20
% F	64.9	52.8	60
a/Å	5.527 (4)	5.55(1)	5.53
b/Å	7.698 (8)	7.75 (2)	7.7
c/Å	5.371 (5)	5.36(1)	5.34
V/$Å^3$	228.52	230.26	228.34
Crystallite size	57 nm	6.8	-
Micro-strains %	0.26	0.31	-
Chi Square	6.83E-6	1.76E-5	-

metal for $NaNiF_3$ vs Na/Na^+ degradation through XRD evaluation, aluminum was replaced with nickel foam collector.

The electrochemical experiments consisted of three-electrode Swagelok-type cells assembled using sodium metal disks with 9 mm of diameter as both reference and counter electrodes. The cells were assembled into a glove box under an argon atmosphere and controlled O_2 and H_2O traces. A 1 M $NaClO_4$ solution in propylene carbonate (PC) was used as the electrolyte and 2% of fluoroethylene carbonate (FEC) was added to the electrolyte to stabilize the interphase. This solution was soaked in two fiberglass (GF/ A-Whatman) disks of the same diameter to act as separators. The cells were controlled in a BioLogic multichannel system. Cyclic voltammetry (CV) was performed at a scan rate of 0.5, 2.5, 10, 15, and 20 mV s^{-1} in the 0.1-4.5 V vs Na^+/Na potential window with 4 sweeps by rate. Galvanostatic discharge-charge cycles were performed at a constant C rate of C/10 between 0.01 and 3.5V. Finally, the capacitive contribution analysis of the NNF+C electrodes with nickel foam collector was included from cyclic voltammetry results as well as C-rate performance at C/10, C/2, C, and C/10. However, in Fig. S6 of the supporting information file, an additional analysis of NNF+C with an aluminum collector was incorporated as well.

3. Results and discussion

$NaNiF_3$ exhibits an orthorhombic structure belonging to the Pnma space group [33], in which Ni atoms form chains parallel to the b-axis, and the corner-sharing NiF_6 octahedra are tilted to define an 8-fold coordination polyhedron for the sodium ions, as shown in Fig. 1. $NaNiF_3$ exhibits a tolerance factor of c.a. 0.82. Both the experimental and theoretical XRD patterns of NNF+C are shown in Fig. 2 evidencing the high purity of the synthesized product.

The calculated unit cell dimensions shown in Table 1 agreed well with the literature values [33]. The crystallite size of NNF +C, calculated from the XRD line broadening analysis method [34], was c.a. 6.8 nm with a corresponding micro-strain% of 0.31. The pristine material without incorporation of sodium citrate (NNF) is reported in Table 1 and supporting information. NNF had a similar lattice parameter to the theoretical Pnma structure and NNF+C. However, the main difference between NNF and NNF+C is its crystallite size of around 57 nm. This

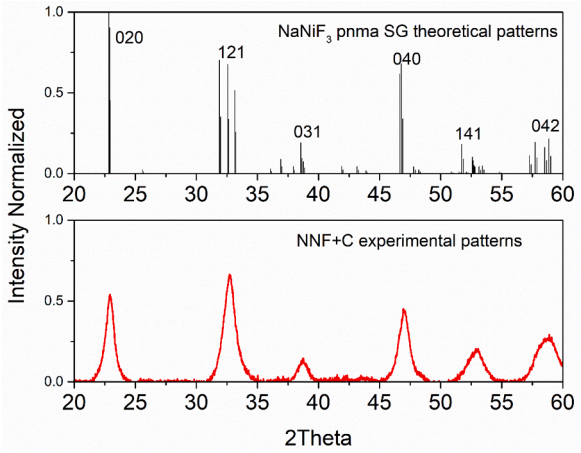

Fig. 2. Experimental XRD patterns of the studied samples NNF+C, and the indexed pattern.

important reduction in crystallite size results from the presence of citrate, which also generated a carbon-coated material, thus explaining the presence of a less crystalline material in the XRD pattern of Fig. 2. At this point, it is worth mentioning that the use of microwave heating was fundamental for the obtention of reduced-size particles, as demonstrated by Hussain et al. [31]. They used the three-sodium citrate as well by oven heating and obtained particles with a clean morphology although their sizes were around 1000 nm.

The Rietveld refinement of NNF and NNF+C pristine materials using the Pnma space group of $NaNiF_3$ structure are presented in Figs. S1 and S2 respectively. Here a good fitting is observed for both materials with low residuals and a Goodness of fit c.a. 0.85 for NNF refinement and 0.70 for NNF+C.

XPS spectroscopy is a helpful technique to unveil the chemical state of elements. Fig. 3 shows the survey spectrum of NNF+C, in which the characteristic transitions are labeled. Also, the sub-spectra at the C1s, Na1s, F1s, and Ni2p core levels are displayed. The C1s spectrum gathers information about the carbon coating and can be deconvoluted into four

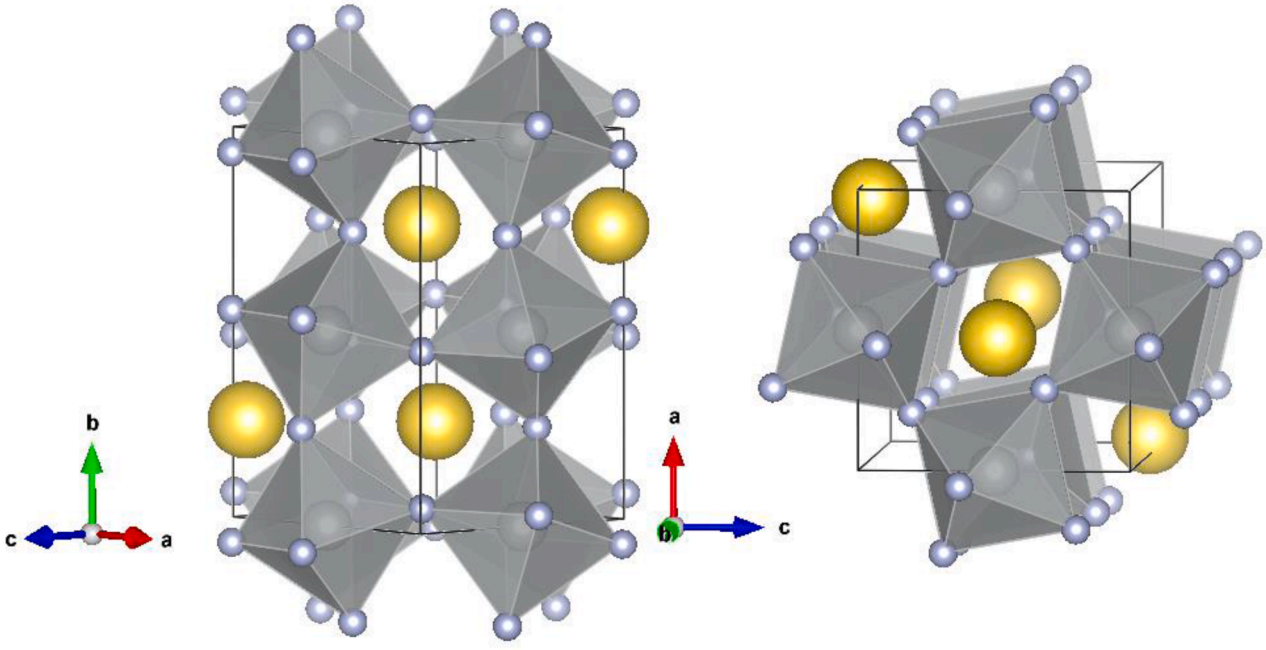

Fig. 1. Two different projections of the orthorhombic structure of $NaNiF_3$. Yellow spheres: Na, small grey spheres: F, larger grey spheres: Ni. The orientation is given by the corresponding unit cell vectors.

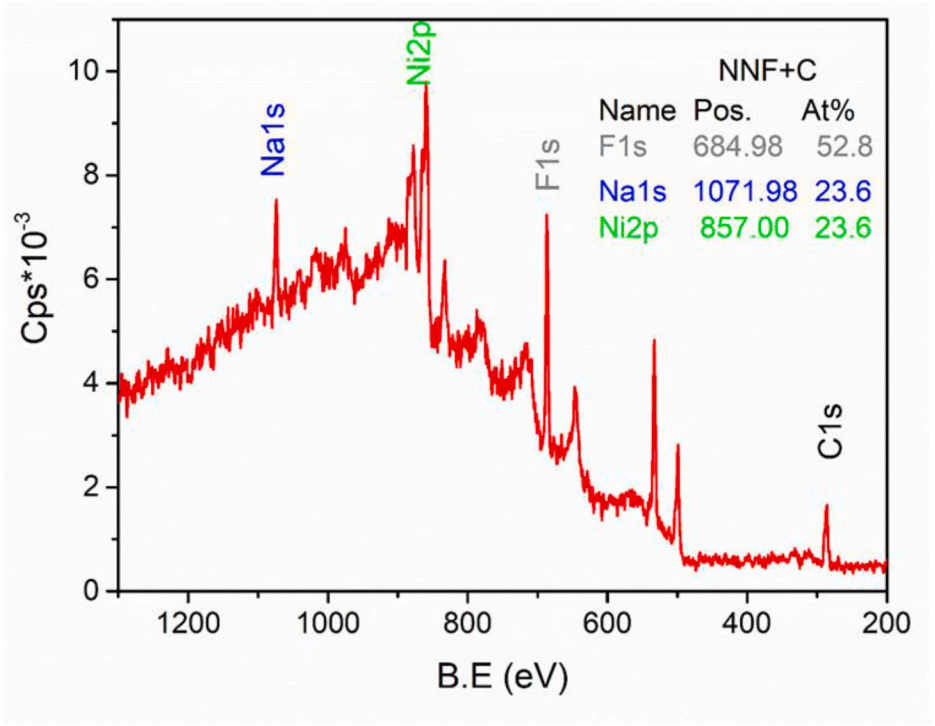

a.

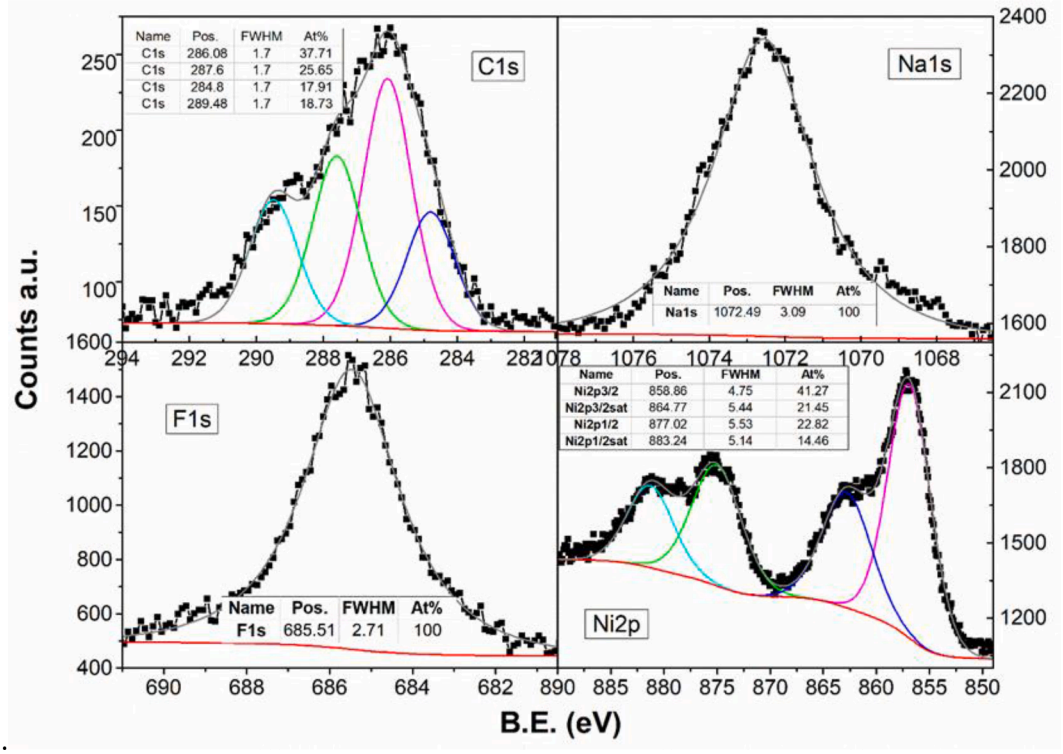

b.

Fig. 3. XPS spectra of NNF+C synthesized material, (a) survey spectrum, and (b) spectra at the C1s, Na1s, F1s, and Ni2p core levels.

f Gaussian- Lorentzian components whose chemical shifts are attributed to graphitic carbon with sp^3 configuration at 284.6 eV, C–OH groups at 285.9 eV, C=O (287.4 eV), and carboxylic groups at 289.3 eV [35].

The Ni2p XPS spectrum revealed two bands that correspond to two-spin orbit doublets of $Ni2P_{3/2}$ and $Ni2P_{1/2}$ at binding energies of 856 and 876 eV respectively with its corresponding satellites, these values fit well with nickel with an oxidation state of Ni^{2+}. In the F1s spectrum, only one band is identified over 685.6 eV which is close to that of related metal fluorides [36]. Finally, the Na1s spectrum showed a band close to 1,072 eV. The preceding signal fits well with the electronic

configuration of $NaNiF_3$.

In addition, the atomic composition determined by the quantification of the XPS spectra of NNF+C is shown in Table 1 and Fig. 3. It evidences a small deviation between the experimental and theoretical values, which could be attributed to the incorporation of the carbon material from citrate sodium. Otherwise, the atomic composition for NNF shown in Table 1 and Fig. S4 was proximate to the theoretical value. Additionally, the XPS spectrum of NNF (Fig. S4) corresponds well to the orbitals and binding energies of Ni2p, Na1s, and F1s from NNF+C (Fig. 3).

Scanning electron micrographs of NNF perovskite active material are shown in Fig. S3. It was evidenced rotund aggregates of primary particles type spheres (Fig. S3a-b), which can be distinguished by TEM (Fig. S3a image with a conformation of clusters and primary spheres with size lower than 100 nm. However, for sodium citrate addition in NNF + C sample, the size of the aggregates decreases with apparent inter-connection between each particle (See Fig. 4a-b) and the primary NNF + C particle size is around 8 nm (Fig. 4h) which fitted well to crystallite size reported in Table 1. The interconnection between each particle is promoted by a carbonous material from the citrate component showing a distribution around the surface of perovskite particles of NNF+C active material. Which apparently works as a matrix where the perovskite particles are embedded and interconnected.

Chemical composition maps were done by STEM for a selected particle of the active materials, such as those shown for NNF+C in Fig. 4c-g, and NNF in Fig. S3 c-f. These were recorded to evidence a uniform elemental distribution of sodium, nickel, and fluorine in the particles. Although all mapping outline in both samples for Na, Ni and F are very similar, it may be observed that mainly the pattern of Ni and F atoms are more similar between each other than Na pattern what could be associated with the bonding between Ni and F elements and their octahedral conformation. To confirm the carbonous component present on the surface of the NNF+C perovskite, a particle was suspended over a hole of the graphite membrane in the copper TEM grid, for what, in Fig. 4d, the presence and uniform distribution of the carbonous component around the surface of perovskite particles with some points with higher carbon concentration is evident.

Fig. 5 a and b show the discharge and charge profiles for the NNF+C

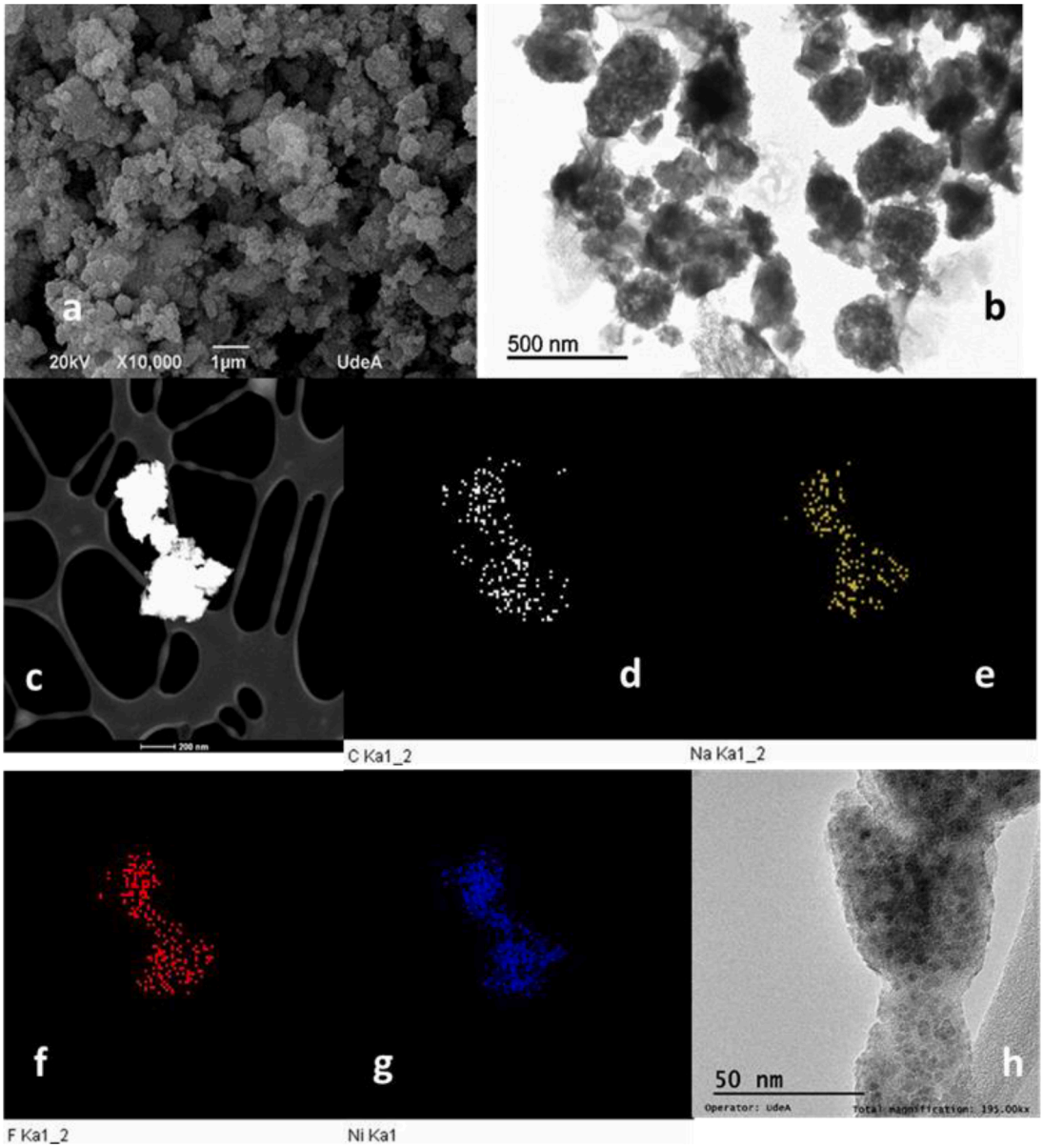

Fig. 4. Micrographs of NNF+C pristine. (a). SEM at 10Kx (1μm), (b). TEM at 20Kx (500 nm). (c-g). contrasted STEM mapping, (d). Carbon, (e). Sodium, (f). Fluorine, (g). Nickel, and (h). TEM at 195 Kx(50nm).

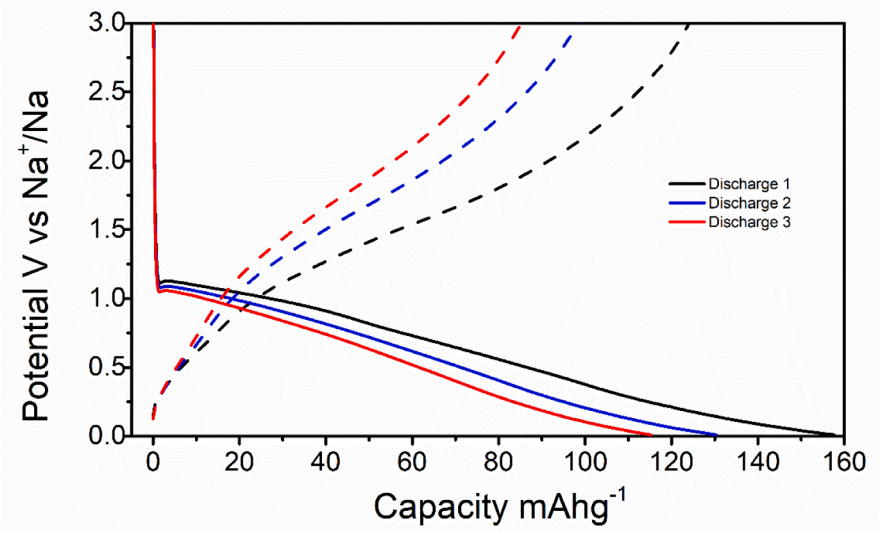

a.

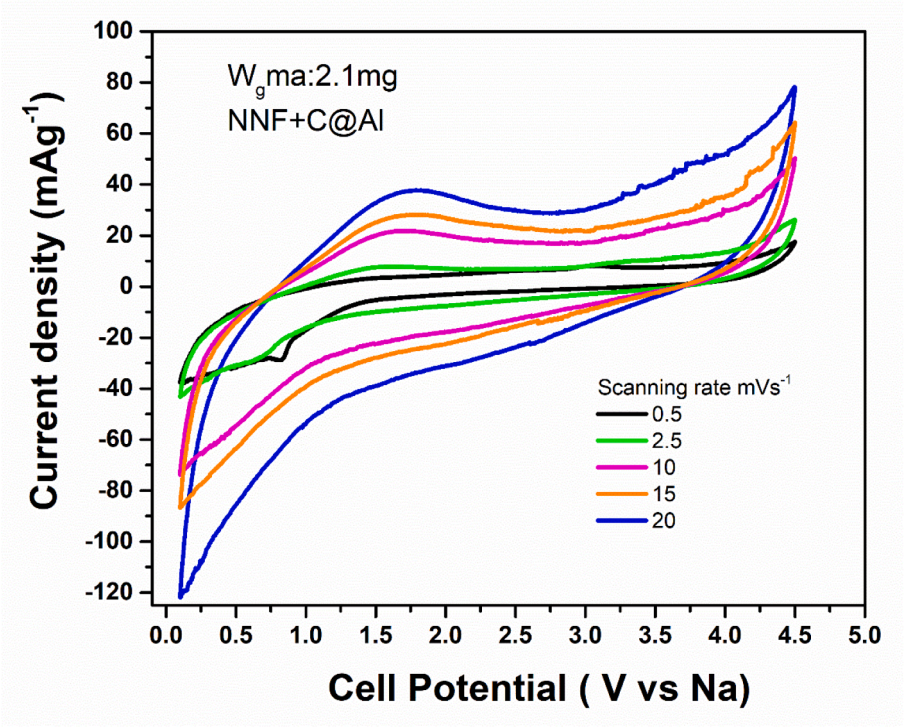

b.

Fig. 5. (a). Discharge-Charge profile of NNF+C@Al electrode, and (b). Voltammetry curves of NNF+C@Al at 0.5, 2.5, 10, 15 and 20 mV s^{-1}.

electrode supported on the aluminum collector for the first three cycles and the cyclic voltammetry in a potential range between 0.1-4.5 V and sweep rates of 0.5, 2.5, 10, 15 and 20 mV s-1 respectively. The discharge capacity obtained in Fig. 5a is close to 160 mA h g-1, which decreases after each cycle. Despite the loss of capacity during cycling, the electrochemical response of the active material is significantly improved, as compared to previous reports in the literature [22,26], which showed lower capacities and poor cyclability.

That behavior was attributed to the low ability of the active material to participate in intercalation reactions. For that purpose, the Ni^{2+}/Ni^{3+} redox couple would require the formation of NiF_3 during the charging process, which does not seem to perform a good electrochemical behavior because it tends to decompose releasing F_2. On the other hand, the voltammetry curve in Fig. 5b does not show apparent redox peaks ascribable to faradaic processes in the cathodic sweep but shows a capacitive behavior.

A maximum specific capacity of 160 mA h g^{-1} was reached (Fig. 5), which is significantly lower than the expected theoretical capacity (386.5 mA h g^{-1}) when conversion processes are carried out with the active material $NaNiF_3$. To gain further information on the origin of this poor electrochemical response observed for the NNF+C material using aluminum as a collector, the ex-situ XRD patterns were recorded on the electrodes after cycling, as shown in Fig. 6. In Fig. 6a, the discharge process is followed by XRD evaluation of the electrode before cycling (red curve), and after different polarization voltages during the first discharge (1V, 0.5V, and 0.1V), which are compared with the electrodes

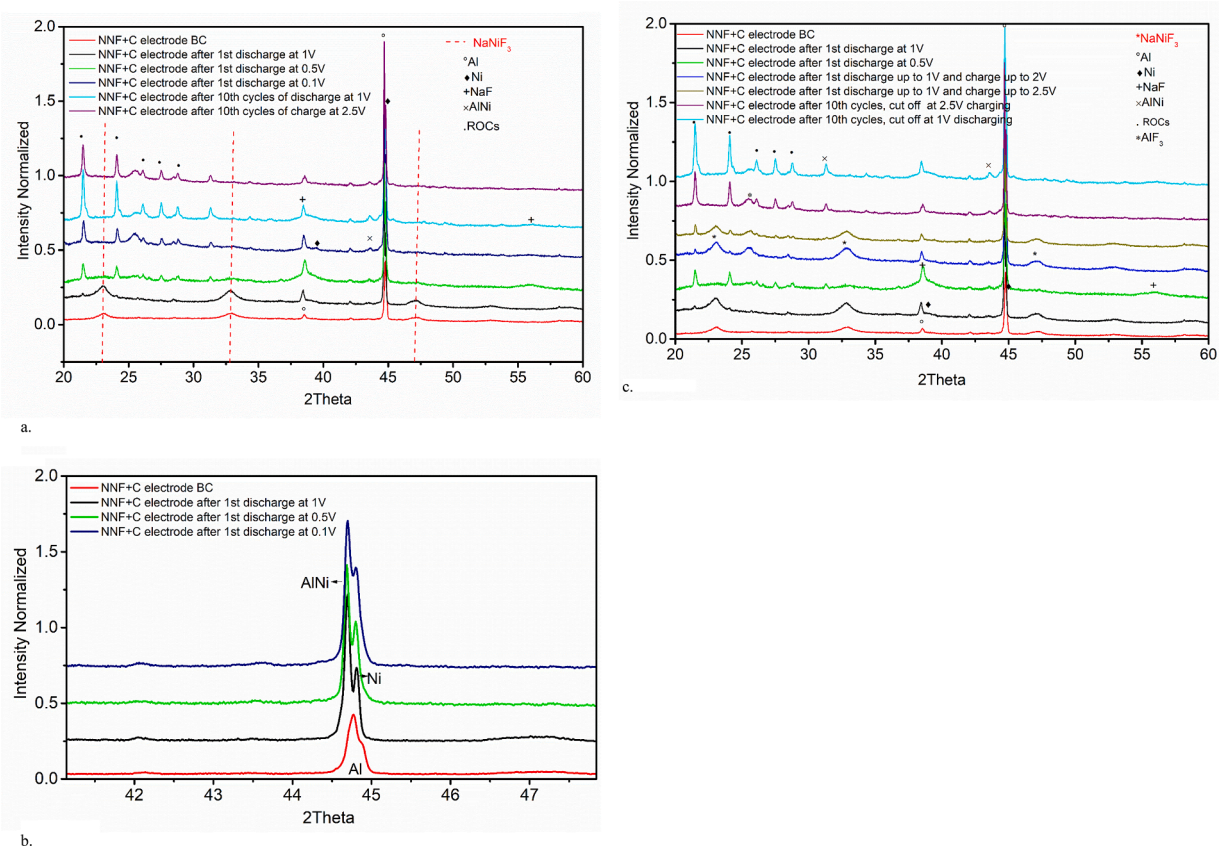

Fig. 6. ex-situ XRD analysis of used electrodes of NNF+C active material over aluminum collector, (a) Through the discharge processes, (b) Zoom of (a) between 42-47° for selected electrodes to observe Ni° and the AlNi Alloy, and (c) Through the charging processes.

that were cycled for 10 times, in voltages between 0.1V-3.2V, cutting the last discharge at 1V (cyan curve) and a cut during the last charge at 2.5V (purple curve). While Fig. 6c focuses on the charging processes for which the analysis of the discharged electrode up to 1 V was added, which is subsequently charged up to 2V (blue curve), and an electrode discharged up to 1V that was subsequently charged up to 2.5 V (gray curve).

During the discharge the presence of the active material $NaNiF_3$ in the red curve is identified, see Fig. 6a, evidencing the main peaks of the structure with the dotted red lines at 23, 32.9, and 47.11 °, when the discharge process begins at 1V (black curve). The greatest variation presented is identified in the increase in intensity and amplitude of a peak at 38.5° which corresponds to the formation of NaF, which intensifies when continuing the discharge at 0.5V (green curve), and the signal at 56° ascribable to the same material being clearer.

However, the amplitude of the peak at 38.5° deepens further because of the formation of the Ni°, which is identified at 39.5° when the discharge of the electrode is carried up to 0.1V. However, at this same voltage, the simultaneous formation of the AlNi alloy is confirmed. As for the permanence of the perovskite structure, it was confirmed that at 1V the structure is still stable. However, when the voltage is reduced to 0.5V, the permanence of the main peaks of $NaNiF_3$ is scarcely identified. In Fig. 6b the formation of Ni° is evidenced from the beginning of the discharge at 1 V, with the formation of a peak at 44.8°. However, the participation of the aluminum collector in the simultaneous alloy with the Ni° to form AlNi is evidenced by the peak at 44.7°. When the discharge of the electrode is carried up to 0.1V, the formation of this alloy seems to be irreversible, given the retention of the peak at 43.5° corresponding to the AlNi alloy in the state of charge at 2.5V (purple curve).

These facts could explain the low reversible capacity of the active material when is supported on an Al collector. However, its intensity is lower compared to the cyan curve to the state of discharge in 1V. In Fig. 6c, the state of charge is studied with different cutting voltages. The first analysis focuses up to a point of discharge at 1V and starting from there the load up to 2 and 2.5 V curve blue and gray respectively. In these curves, the presence of $NaNiF_3$ and the decrease in intensity of the peak by 38.5° that would correspond to the NaF when going from 2 to 2.5V are evident. In addition, the amplitude (observed as a belly) of this same peak is no longer identified at 2.5V compared to discharge (black curve) at 1V or discharge at 0.5V (green curve). This could indicate that the NaF and Ni° formed during reduction at 1 V could reverse to $NaNiF_3$ formation. However, in the oxidation state (loading process) the formation of characteristic AlF_3 was also identified at 25.6° as clearly shown in the purple curve which corresponds to 10 cycles between 0.1V and 3.2V whose cutting was made during the last load at 2.5V. However, it seems that this product is a little reversible since its presence is identified in the cyan curve that corresponds to 10 cycles between 0.1V and 3.2V whose cutting was made during the last discharge at 1V. Right here we can see the great difference in bringing the discharge up to 0.1 V (purple curve) to bringing the discharge up to 1V at the same charging point to 2.5V (gray curve) due to the non-reversibility and complete disappearance of $NaNiF_3$, which could be due in part to the quasi-irreversible formation of the AlNi alloy during discharge at low voltages and the formation of AlF_3 during charging.

The above results prompted us to evaluate the stability of an electrode of the active material NNF+C when using an Al-free current collector. For this purpose, nickel foam was chosen as an alternative current collector to avoid the formation of AlNi alloys and the AlF_3 compound, as shown in Fig. 7.

The electrochemical response of the active material supported on nickel foam NNF+C @Nf was considerably improved. An initial capacity value of 940 mA h g^{-1} was obtained and associated with solid electrolyte

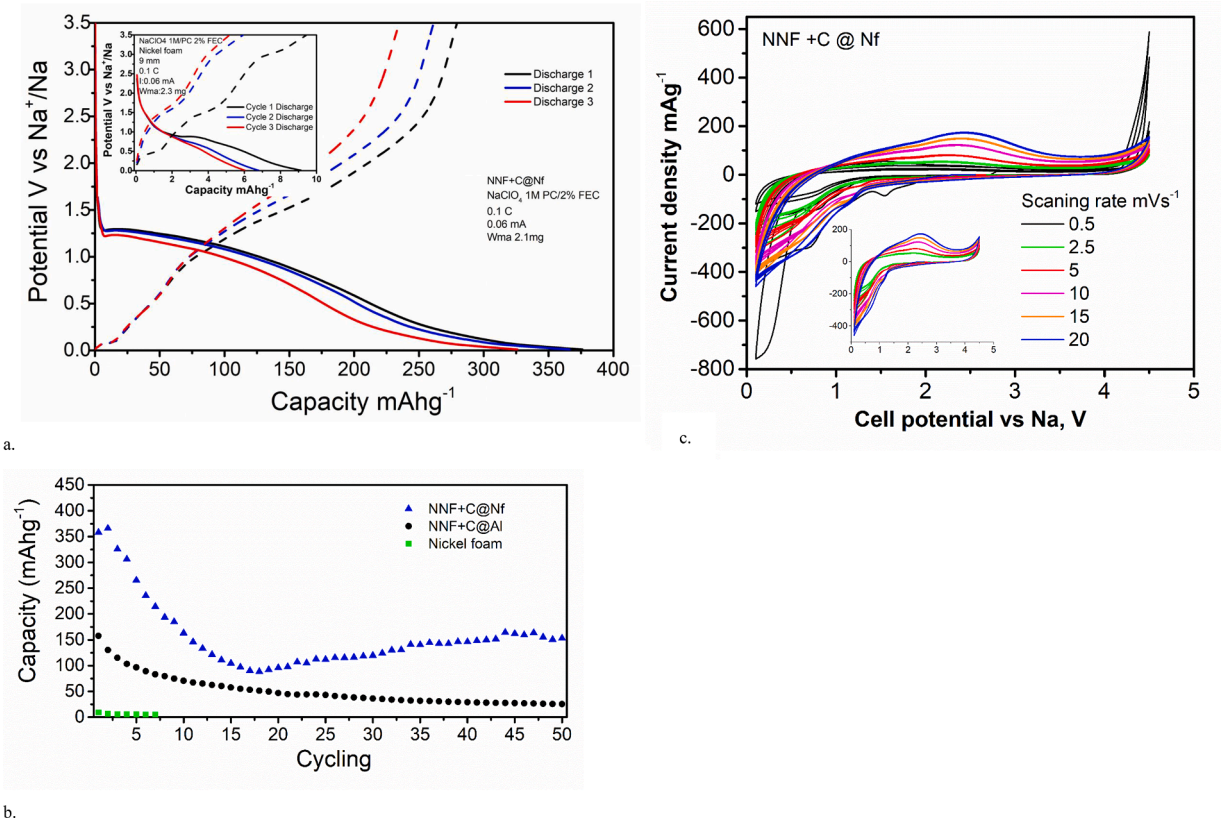

Fig. 7. (a). Discharge-Charge profile of NNF+C@Nf electrode during the three first cycles, (b). Cycling curve of NNF+C@Nf, NNF+C@Al and Nickel foam electrodes, and (c). Voltammetry curves of NNF+C@Nf at 0.5, 2.5, 10, 15, and 20 mV s^{-1}.

interphase - SEI formation (it was not included in the graphic information). The SEI formation consumes sodium from the active material as well as from the electrolyte [37,38], which explains the higher capacity during the initial discharge. Further to SEI formation, the material displayed a first capacity of discharge around 376 mA h g^{-1}, which is close to its theoretical capacity of 386.5 mA h g^{-1}, in agree with the conversion reaction, as can be seen in Fig. 7a. In addition, the coulombic efficiency reached was 73%.

The capacity remained close to 170 mA h g^{-1} at the 50th cycle. That behavior is attributed to the increase of the electroactive area of the material in contact with the electrolyte due to the good electrical conductivity of the nickel foam. Besides it was confirmed according to the inset in Fig. 7a, that the nickel foam as electrode did not have enough contribution to capacity vs Na^+, because it obtained a first discharge capacity of only 8 mA h g^{-1}. The electrode conserves a uniform coat of the material even after cycling, which means the morphology of the foam support well the constant change of volume of the structures of the active material during cycling as can be seen in Fig. S5, in the supporting information. Similarly, the greater stability and capacity of the electrode supported on nickel foam compared to that supported on aluminum is due to the non-formation of aluminum-secondary products such as AlNi alloys and AlF_3, which leads to the apparent degradation of the active material. Also, the capacity retention of the active material on the nickel foam current collector at the 50th cycle reached almost 45% of the initial capacity (NNF+C@Nf), which is a superior to the value of 13% obtained when the Al collector was used (NNF+C@Al), see Fig. 7b.

Irrespective of the collector, it was observed that the incorporation of sodium citrate optimized the material microstructure and improved the energy efficiency of sodium-ion batteries due to the decrease in particle size, which is an important factor that can contribute to improving the electrochemical activity in the conversion materials [28].

On the other hand, a marked polarization of the active material occurs, as can be seen in Fig. 7a-c. The polarization effect can be attributed to a large ohmic drop induced by the big surface energy contribution related to the formation of Ni metal nanocrystals, which was visible in all XRD patterns measured during the discharge experiments in Fig. 6a, as well as compositional inhomogeneity process. The ohmic drop can be caused by the M−F bonds having an ionic character which displayed a weak electrical conductivity in perovskite material and caused a poor electrochemical performance related to the high insulating character of fluorides [25,39]. Nevertheless, the nickel foam improved the initial capacities and capacity retention of the electrode material, as it facilitated an increase in interface connectivity once the first reduction has taken place [30]. The large polarization is also clearly visible by cyclic voltammetry (Fig. 7 c), which was performed at sweep rates of 0.5, 2.5, 5, 10, 15, and 20 mV s^{-1} with four repetitions each. The main cathodic and anodic waves occur at ca. 1.2 and 2.4V vs Na^+, respectively. Having in mind the next reaction:

$$NaNiF_3 + 2Na \rightarrow Ni + 3NaF \quad (1)$$

The enthalpy associated with (1) reaction and calculated from the formation enthalpy of Na and $NaNiF_3$ with the data available on the Materials Project website [40] is c.a. -4.72 eV which leads to an expected electrochemical potential of 2.35 V. What differs from the experimental discharge values. The kinetic hindrance is responsible for a decrease of ca 0.8 V in discharge.

According to the evidence shown during the analysis of ex-situ XRD (Fig. 6), where the formation of Ni and NaF were confirmed, the following conversion reactions could be expressed as:

During the first discharge:

$$NaNiF_3 + 2Na^+ + 2e^- \rightarrow Ni + 3NaF \quad (2)$$

For the charge step, probably the next reaction might occur,

$$NaNiF_3 + 2Na^+ + 2e^- \leftarrow Ni + 3NaF \quad (3)$$

The reaction (3) seems to be not completely reversible, which probably contributes to the capacity retention loss during cycling. This result confirmed the feasibility of the conversion mechanism [41,42] proposed in this work to explain the electrochemical performance of the $NaNiF_3$ active material during the cycling of the semi cells vs Na^+/Na. At the same time, it was dismissed any likelihood to carried out an intercalation mechanism, what would require a high reaction enthalpy of 5.71 eV (551 KJ mol $^{-1}$) for the formation of NiF_3 what structurally is not favorable, and here an unpractical operation voltage c.a. 5.7 V vs Na^+ would be expected. The obtained C-rate curves in Fig. 8a had similar behavior to other perovskite electrode materials with a reaction mechanism by conversion [43], where good reversibility is obtained at higher current densities.

Although, according to the lack of coulombic efficiency and the rapid capacity decay during cycling, there may be some destabilizations of the SEI film and a resulting electrolyte reduction would be expected too, according to a second peak of reduction around 0.75V vs Na^+, which was observed in Fig. 7c. For that reason, exploring additional strategies to conserve the steadiness of the SEI and the accurate choice of electrolyte and its concentration could be fundamental to increase the stabilization of this type of electrode material.

Finally, the voltammetry curves observed in Figs. 5b and 7c for the NNF+C material supported on Al and nickel foam substrates, respectively, indicate the existence of a capacitive behavior of the charge/discharge processes. For this reason, a more detailed voltammetric analysis was done to verify the different current density contributions. As can be seen in Fig. 8b-d, there was a capacitive contribution to the electrochemical activity of the active material. By reducing the size of the crystallite to a nanoscale dimension, the stored capacity could be affected [44]. Thus, an increase in specific surface area allows two different electrochemical contributions such as faradaic and capacitive [45–47].

The capacitive effect was evaluated according to the following expression:

$$i = av^b$$

Where the measured current i obeys a power-law relationship with the sweep rate υ. Both a and b are adjustable parameters, with b-values determined from the slope of the plot of log i vs log υ shown in Fig. 8b. There are two well-defined conditions: b = 0.5 and b = 1.0. For b = 0.5, the current response is diffusion-controlled, which is indicative of a faradaic process. While the b=1 or closer, this is representative of a capacitive response, and here the capacitive current is proportional to the sweep rate according to the next equation:

$$i = vC_dA$$

Where C_d is the capacitance and A is the surface area of the electrode materials. To distinguish quantitatively capacitive contribution to the

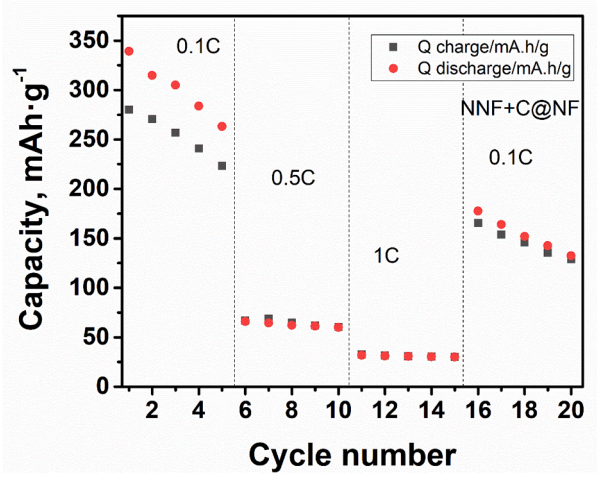

a.

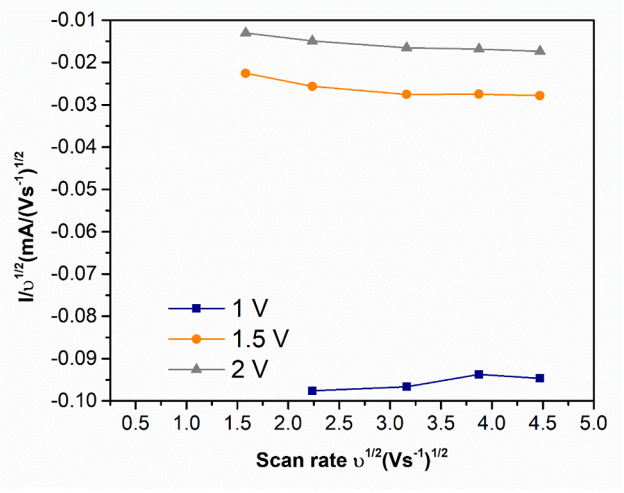

c.

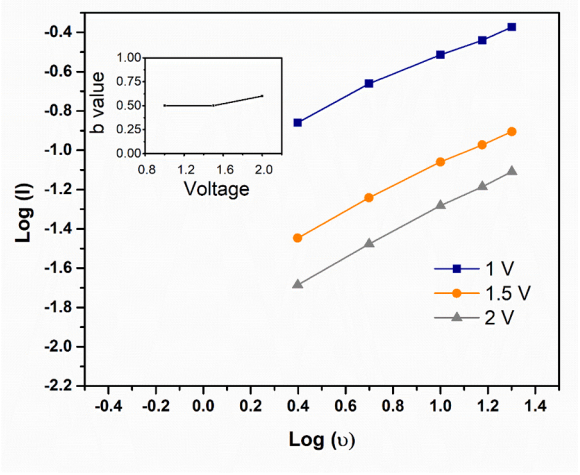

b.

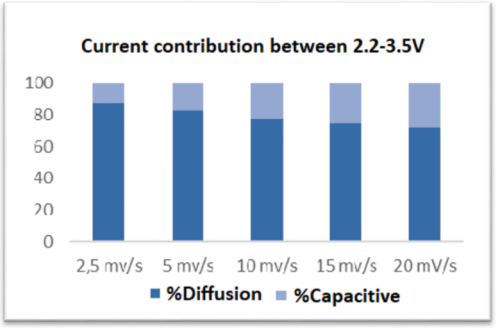

d.

Fig. 8. (a). C-rate analysis at 0.1, 0.5, 1 C of NNF+C@Nf electrode during 5 cycles by current, (b). Log (I) vs Log (v) of NNF+C@Nf electrode at 1V, 1.5, and 2V, (c). Analysis of cathodic voltammetric sweep data for NNF+C@Nf electrode, and (d). Current contribution for NNF+C@Nf electrode.

current response at a fixed potential, two separated mechanisms of surface capacitive effects and diffusion-controlled processes can be expressed with the following expression:

$$i(V) = k_1 v + k_2 v^{1/2}$$

That can be rearranged as:

$$i(V)/v^{1/2} = k_1 v^{1/2} + k_2 v$$

k_1* υ and k_2* $\upsilon^{1/2}$ correspond to the current contributions from the surface capacitive effects and the diffusion-controlled intercalation process, respectively, and these were evaluated in Fig. 8c. When k_1 and k_2 are determined, it is possible to quantify, at specific potentials, the fraction of the current due to each contribution that was analyzed in Fig. 8d. Here was observed that for NNF+C over Nickel foam, there is a primarily faradaic process due to the b value being close to 0.5 with some diffusion control; however, as well capacitive contribution over the total current is identified with an increase from 10% at 2.5mV s^{-1} up to 25% at 20 mV s^{-1}, that probe that $NaNiF_3$ active material has faradaic and capacitive contributions to the total stored charge. The same analysis with similar results was done for the NNF+C with aluminum collector observed in Fig. S7, which could permit us to conclude the capacitive contribution exclusively obeys to active material nature.

4. Conclusion

In this work, we obtained $NaNiF_3$ perovskite with an optimized microstructure from the use of sodium citrate and microwave heating as electrode material for sodium-ion batteries on nickel foam as a current collector. The process started by discharge seemingly leads to the conversion reaction. Here a remarkable first discharge capacity of c.a. 376 mA h g^{-1} was obtained with a retention of c.a. 45% during 50th cycle. The proposed conversion mechanism involves the formation of Ni and NaF compounds during the first discharge process. The conversion reaction seems to be not completely reversible, which probably contributes to the capacity retention loss during cycling. Besides a capacitive contribution to total charge of c.a. 25% was identified over the evaluated active material between 2.2V-3.5V at 20mV s^{-1}.

CRediT authorship contribution statement

Liliana T. López Ch: Investigation, Validation, Writing – original draft. **Alejandro Medina:** Investigation, Validation, Writing – original draft. **Franklin Jaramillo:** Conceptualization, Writing – review & editing. **Jorge A. Calderón:** Conceptualization, Methodology, Funding acquisition, Writing – review & editing. **Pedro Lavela:** Conceptualization, Writing – review & editing. **José L. Tirado:** Conceptualization, Methodology, Funding acquisition, Writing – review & editing.

Declaration of Competing Interest

The authors declare that they have no known competing financial interests or personal relationships that could have appeared to influence the work reported in this paper.

Acknowledgments

The authors are grateful to Universidad de Córdoba and European Region Development Funds (grant UCO-FEDER 20 ref. 1390025-R), and Consejería de Economía, Innovación, Ciencia y Empleo, Junta de Andalucía (grant FQM288). We also thank SCAI (UCO Central Service for Research Support) for chemical analysis, XPS spectroscopy and electron microscopy. LTLC is grateful to Fundación Carolina for grant Segib 2020 for the exchange program, to Universidad de Antioquia and the financial support in Colombia from Colombia Scientific Program within the framework of the call Ecosistema Científico (Contract FP44842-218-2018).

Supplementary materials

Supplementary material associated with this article can be found, in the online version, at doi:10.1016/j.electacta.2023.142341.

References

[1] P.V. Kamat, Lithium-ion batteries and beyond: celebrating the 2019 Nobel Prize in Chemistry - a virtual issue, ACS Energy Lett. (2019) 2757–2759, https://doi.org/10.1021/acsenergylett.9b02280.
[2] V. Palomares, M. Casas-Cabanas, E. Castillo-Martínez, M.H. Han, T. Rojo, Update on Na-based battery materials. A growing research path, Energy Environ. Sci. 6 (2013) 2312–2337.
[3] M.D. Slater, D. Kim, E. Lee, C.S. Johnson, Sodium-ion batteries, Adv. Funct. Mater. 23 (2013) 947–958.
[4] H. Pan, Y.-S. Hu, L. Chen, Room-temperature stationary sodium-ion batteries for large-scale electric energy storage, Energy Environ. Sci. 6 (2013) 2338–2360.
[5] S. Kim, D. Seo, X. Ma, G. Ceder, K. Kang, Electrode materials for rechargeable sodium-ion batteries: potential alternatives to current lithium-ion batteries, Adv. Energy Mater. 2 (2012) 710–721.
[6] D. Saurel, B. Orayech, B. Xiao, D. Carriazo, X. Li, T. Rojo, From charge storage mechanism to performance: a roadmap toward high specific energy sodium-ion batteries through carbon anode optimization, Adv. Energy Mater. 8 (2018), 1703268.
[7] P.K. Nayak, L. Yang, W. Brehm, P. Adelhelm, From lithium-ion to sodium-ion batteries: advantages, challenges, and surprises, Angew. Chemie - Int. Ed. 57 (2018) 102–120, https://doi.org/10.1002/anie.201703772.
[8] A. Bauer, J. Song, S. Vail, W. Pan, J. Barker, Y. Lu, The scale-up and commercialization of nonaqueous Na-ion battery technologies, Adv. Energy Mater. 8 (2018) 1–13, https://doi.org/10.1002/aenm.201702869.
[9] Y. Li, Y. Lu, C. Zhao, Y.S. Hu, M.M. Titirici, H. Li, X. Huang, L. Chen, Recent advances of electrode materials for low-cost sodium-ion batteries towards practical application for grid energy storage, Energy Storage Mater. 7 (2017) 130–151, https://doi.org/10.1016/j.ensm.2017.01.002.
[10] M. Arnaiz, J.L. Gómez-Cámer, E. Gonzalo, N.E. Drewett, J. Ajuria, E. Goikolea, M. Galceran, T. Rojo, Exploring Na-ion technological advances: pathways from energy to power, Mater. Today Proc. (2020), https://doi.org/10.1016/j.matpr.2020.03.704.
[11] S. Rubio, R.R. Maça, M.J. Aragón, M. Cabello, M. Castillo-Rodríguez, P. Lavela, J. L. Tirado, V. Etacheri, G.F. Ortiz, Superior electrochemical performance of TiO2 sodium-ion battery anodes in diglyme-based electrolyte solution, J. Power Source. 432 (2019) 82–91, https://doi.org/10.1016/j.jpowsour.2019.05.070.
[12] M. Tathavadekar, S. Krishnamurthy, A. Banerjee, S. Nagane, Y. Gawli, A. Suryawanshi, S. Bhat, D. Puthusseri, A.D. Mohite, S. Ogale, Low-dimensional hybrid perovskites as high performance anodes for alkali-ion batteries, J. Mater. Chem. A. 5 (2017) 18634–18642.
[13] M. Cabello, X. Bai, T. Chyrka, G.F. Ortiz, P. Lavela, R. Alcántara, J.L. Tirado, On the reliability of sodium Co-intercalation in expanded graphite prepared by different methods as anodes for sodium-ion batteries, J. Electrochem. Soc. 164 (2017) A3804–A3813, https://doi.org/10.1149/2.0211714jes.
[14] L.T. López, D. Ramírez, F. Jaramillo, J.A. Calderón, Novel hybrid organic-inorganic CH3NH3NiCl3 active material for high-capacity and sustainable lithium-ion batteries, Electrochim. Acta. (2020) 357, https://doi.org/10.1016/j.electacta.2020.136882.
[15] Y. Yamada, T. Doi, I. Tanaka, S. Okada, J.I. Yamaki, Liquid-phase synthesis of highly dispersed NaFeF3 particles and their electrochemical properties for sodium-ion batteries, J. Power Source. 196 (2011) 4837–4841, https://doi.org/10.1016/j.jpowsour.2011.01.060.
[16] T. Kim, W. Song, D.-Y. Son, L.K. Ono, Y. Qi, Lithium-ion batteries: outlook on present, future, and hybridized technologies, J. Mater. Chem. A. 7 (2019) 2942–2964.
[17] H. Tanaka, T. Oku, N. Ueoka, Structural stabilities of organic–inorganic perovskite crystals, Jpn. J. Appl. Phys. (2018) 57, https://doi.org/10.7567/JJAP.57.08RE12.
[18] J.A. Dawson, A.J. Naylor, C. Eames, M. Roberts, W. Zhang, H.J. Snaith, P.G. Bruce, M.S. Islam, Mechanisms of lithium intercalation and conversion processes in organic–inorganic halide perovskites, ACS Energy Lett. 2 (2017) 1818–1824, https://doi.org/10.1021/acsenergylett.7b00437.
[19] N. Vicente, D. Bresser, S. Passerini, G. Garcia-Belmonte, Probing the 3-step lithium storage mechanism in CH3NH3PbBr3 perovskite electrode by operando-XRD analysis, ChemElectroChem (2018), https://doi.org/10.1002/celc.201801291.
[20] D. Ramirez, Y. Suto, N.C. Rosero-Navarro, A. Miura, K. Tadanaga, F. Jaramillo, Structural and electrochemical evaluation of three- and two-dimensional organohalide perovskites and their influence on the reversibility of lithium intercalation, Inorg. Chem. 57 (2018) 4181–4188, https://doi.org/10.1021/acs.inorgchem.8b00397.
[21] H.-R. Xia, W.-T. Sun, L.-M. Peng, Hydrothermal synthesis of organometal halide perovskites for Li-ion batteries, Chem. Commun. 51 (2015) 13787–13790.
[22] I.D. Gocheva, M. Nishijima, T. Doi, S. Okada, J. Yamaki, T. Nishida, Mechanochemical synthesis of NaMF3 (M= Fe, Mn, Ni) and their electrochemical properties as positive electrode materials for sodium batteries, J. Power Source. 187 (2009) 247–252.

[23] J. Kim, H. Kim, K. Kang, Conversion-based cathode materials for rechargeable sodium batteries, Adv. Energy Mater. 8 (2018), 1702646.
[24] A. Kitajou, Y. Ishado, T. Yamashita, H. Momida, T. Oguchi, S. Okada, Cathode properties of perovskite-type Na M F 3 (M = Fe, Mn, and Co) prepared by mechanical ball milling for sodium-ion battery, Electrochim. Acta. 245 (2017) 424–429, https://doi.org/10.1016/j.electacta.2017.05.153.
[25] A. Martin, M. Doublet, E. Kemnitz, N. Pinna, Reversible sodium and lithium insertion in iron fluoride perovskites, Adv. Funct. Mater. 1802057 (2018) 2–8, https://doi.org/10.1002/adfm.201802057.
[26] N. Dimov, A. Nishimura, K. Chihara, A. Kitajou, I.D. Gocheva, S. Okada, Transition metal NaMF3 compounds as model systems for studying the feasibility of ternary Li-M-F and Na-M-F single phases as cathodes for lithium-ion and sodium-ion batteries, Electrochim. Acta. 110 (2013) 214–220, https://doi.org/10.1016/j.electacta.2013.05.103.
[27] J. Nava-Avendaño, M.E. Arroyo-De Dompablo, C. Frontera, J.A. Ayllón, M. R. Palacín, Study of sodium manganese fluorides as positive electrodes for Na-ion batteries, Solid State Ionics 278 (2015) 106–113, https://doi.org/10.1016/j.ssi.2015.05.023.
[28] L. Li, R. Jacobs, P. Gao, L. Gan, F. Wang, D. Morgan, S. Jin, Origins of large voltage hysteresis in high-energy-density metal fluoride lithium-ion battery conversion electrodes, J. Am. Chem. Soc. 138 (2016) 2838–2848, https://doi.org/10.1021/jacs.6b00061.
[29] L. Zhang, J. Miao, J. Li, Q. Li, Halide perovskite materials for energy storage applications, Adv. Funct. Mater. 30 (2020) 1–20, https://doi.org/10.1002/adfm.202003653.
[30] S. Ni, J. Ma, X. Lv, X. Yang, L. Zhang, Fabrication of NaNiF3/Ni composite and its application in lithium ion batteries, Mater. Lett. 124 (2014) 264–266, https://doi.org/10.1016/j.matlet.2014.03.057.
[31] N. Hussain, F. Wu, W. Younas, L. Xu, Hollow sphere formation by the self aggregation of perovskite fluoride NaNiF3 nanocrystals and the application of these spheres as an electrode in an ultrahigh performance asymmetric supercapacitor, New J. Chem. 43 (2019) 11959–11967, https://doi.org/10.1039/c9nj02221j.
[32] J. Hwang, J. Chun, Microwave-assisted solvothermal synthesis of sodium metal fluoride (NaxMFy) nanopowders, J. Am. Ceram. Soc. 102 (2019) 6475–6479, https://doi.org/10.1111/jace.16702.
[33] F. Pompa, F. Siciliano, Crystallographic distorsions in the ABF 3 compounds, Comitato Nazionale per l'Energia Nucleare (1970).
[34] G.K. Williamson, W.H. Hall, X-ray line broadening from filed aluminium and wolfram, Acta Metall. 1 (1953) 22–31.
[35] M.J. Aragón, J. Gutiérrez, R. Klee, P. Lavela, R. Alcántara, J.L. Tirado, On the effect of carbon content for achieving a high performing Na3V2(PO4)3/C nanocomposite as cathode for sodium-ion batteries, J. Electroanal. Chem. 784 (2017) 47–54, https://doi.org/10.1016/j.jelechem.2016.11.064.
[36] J. Tan, L. Liu, S. Guo, H. Hu, Z. Yan, Q. Zhou, Z. Huang, H. Shu, X. Yang, X. Wang, The electrochemical performance and mechanism of cobalt (II) fluoride as anode material for lithium and sodium ion batteries, Electrochim. Acta. 168 (2015) 225–233, https://doi.org/10.1016/j.electacta.2015.04.029.
[37] P.U. Nzereogu, A.D. Omah, F.I. Ezema, E.I. Iwuoha, A.C. Nwanya, Anode materials for lithium-ion batteries : a review, Appl. Surf. Sci. Adv. 9 (2022), 100233, https://doi.org/10.1016/j.apsadv.2022.100233.
[38] A. Wang, S. Kadam, H. Li, S. Shi, Y. Qi, Review on modeling of the anode solid electrolyte interphase (SEI) for lithium-ion batteries, Nat. Partn. J. (2018) 1–26, https://doi.org/10.1038/s41524-018-0064-0.
[39] D. Ma, H. Wang, Y. Li, D. Xu, S. Yuan, X. Huang, X. Zhang, Y. Zhang, In situ generated FeF3 in homogeneous iron matrix toward high-performance cathode material for sodium-ion batteries, Nano Energy 10 (2014) 295–304.
[40] A. Jain, G. Hautier, S.P. Ong, C.J. Moore, C.C. Fischer, K.A. Persson, G. Ceder, Formation enthalpies by mixing GGA and GGA + U calculations, Phys. Rev. B. 84 (2011), 045115, https://doi.org/10.1103/PhysRevB.84.045115.
[41] P. Poizot, S. Laruelle, S. Grugeon, J.-M. Tarascon, Rationalization of the low-potential reactivity of 3d-metal-based inorganic compounds toward Li, J. Electrochem. Soc. 149 (2002) A1212, https://doi.org/10.1149/1.1497981.
[42] F. Wang, R. Robert, N.A. Chernova, N. Pereira, F. Omenya, F. Badway, X. Hua, M. Ruotolo, R. Zhang, L. Wu, V. Volkov, D. Su, B. Key, M.Stanley Whittingham, C. P. Grey, G.G. Amatucci, Y. Zhu, J. Graetz, Conversion reaction mechanisms in lithium ion batteries: Study of the binary metal fluoride electrodes, J. Am. Chem. Soc. 133 (2011) 18828–18836, https://doi.org/10.1021/ja206268a.
[43] K. Roy, T. Li, S. Ogale, N. Robertson, Hybrid perovskite-like iodobismuthates as low-cost and stable anode materials for lithium-ion battery applications, J. Mater. Chem. A. 9 (2021) 2689–2693, https://doi.org/10.1039/d0ta07414d.
[44] F. Guo, N. Gupta, X. Teng, Enhancing pseudocapacitive process for energy storage devices: analyzing the charge transport using electro-kinetic study and numerical modeling, Supercapacit. - Theor. Pract. Solut. (2018), https://doi.org/10.5772/intechopen.73680.
[45] M.C. López, G.F. Ortiz, P. Lavela, R. Alcántara, J.L. Tirado, Improved coulombic efficiency in nanocomposite thin film based on electrodeposited-oxidized FeNi-electrodes for lithium-ion batteries, J. Alloys Compd. 557 (2013) 82–90, https://doi.org/10.1016/j.jallcom.2012.12.153.
[46] M.C. López, G.F. Ortiz, P. Lavela, R. Alcántara, J.L. Tirado, Improved energy storage solution based on hybrid oxide materials, ACS Sustain. Chem. Eng. 1 (2013) 46–56, https://doi.org/10.1021/sc300096s.
[47] J. Wang, J. Polleux, J. Lim, B. Dunn, Pseudocapacitive contributions to electrochemical energy storage in TiO 2 (anatase) nanoparticles, J. Phys. Chem. C. 111 (2007) 14925–14931, https://doi.org/10.1021/jp074464w.